Korean J. Chem. Eng., 36(11), 1753-1766 (2019)
DOI: 10.1007/s11814-019-0365-0

pISSN: 0256-1115
eISSN: 1975-7220

REVIEW PAPER

A short review on electrochemically self-doped TiO_2 nanotube arrays: Synthesis and applications

Sung Pil Hong[*,‡], Seonghwan Kim[*,‡], Nayeong Kim[*], Jeyong Yoon[*,,†], and Choonsoo Kim[***,†]**

*School of Chemical and Biological Engineering, College of Engineering, Institute of Chemical Process, Seoul National University (SNU), Gwanak-gu, Daehak-dong, Seoul 08826, Korea
**Korea Environment Institute, 370 Sicheong-daero, Sejong-si 30147, Korea
***Department of Environmental Engineering, Kongju National University, 1223-23, Cheonan-daero, Cheonan-si 31080, Korea
(*Received 20 June 2019 • accepted 15 August 2019*)

Abstract−Electrochemically self-doped TiO_2 nanotube arrays (known as reduced TiO_2 nanotube arrays, *r*-TiO_2 NTAs) are currently drawing great attention as emerging and promising materials for energy and environmental applications as they exhibit highly enhanced electrochemical properties, such as good capacitive properties and electro- and photocatalytic activity when compared to pristine TiO_2 NTAs. Such enhanced properties are attributed to the introduction of trivalent titanium ($Ti^{(III)}$) as a self-dopant in the lattice of pristine TiO_2 NTAs through simple electrochemical reduction. However, in spite of the great interest in, and potential of this material, there is no comprehensive review on the synthesis and applications of *r*-TiO_2 NTAs. Therefore, in this review, we critically and briefly review *r*-TiO_2 NTAs in terms of the electrochemical self-doping mechanism, their functional features, and various applications including photolysis, dye-sensitized solar cells (DSSCs), biomedical coatings and drug delivery. In addition, to better understanding *r*-TiO_2 NTAs, pristine TiO_2 NTAs are briefly introduced. Furthermore, this review proposes future research directions with major challenges to be overcome for the successful development of *r*-TiO_2 NTAs, such as to standardize matrices for performance evaluation, to confirm the organic degradation performance as anode, and to improve mechanical stability.

Keywords: TiO_2 Nanotube Arrays (NTAs), Electrochemical Self-doping, Capacitive Property, Electrocatalytic Activity, Photocatalytic Activity

INTRODUCTION

Over the past few decades, highly aligned TiO_2 nanotube arrays (NTAs) have been studied as promising materials for energy and environmental applications [1-3] due to their functional features, such as a highly ordered structure, large surface area, and stability [4-6]. In particular, it is a unique advantage for various applications to achieve well organized nanostructure via simple electrochemical anodization [7] without any need for depositing TiO_2 onto substrates [8]. However, one obstacle to the effective utilization of TiO_2 NTAs is the semi-conductive nature of TiO_2 with a wide bandgap [9,10]. For example, in a solar-driven photocatalytic process, the optical activity of TiO_2 NTAs is limited to the ultraviolet region [11]. The semi-conductive properties of TiO_2 NTAs are also responsible for their poor electrocatalytic activity and low conductivity, which hinders their electrochemical application [12,13]. To overcome problems due to their semi-conductive nature, a number of researchers focused on narrowing the bandgap of TiO_2 NTAs through thermal hydrogenation and incorporation of foreign elements [14-17]. As an alternative technique, electrochemical self-doping is proposed to narrow the bandgap of TiO_2 NTAs under moderate doping conditions [18-23]; this is considered as effective doping strategy to enhance not only the electro- and photocatalytic activity of TiO_2 NTAs but also their capacitive properties [24-28]. In addition, self-doping induces only a small structural distortion [19,29], as it does not require foreign impurities. In this technique, trivalent titanium ($Ti^{(III)}$), produced by electrochemical reduction, serves as the fundamental dopant and plays a critical role in improving the key functional features of TiO_2 NTAs (anatase or amorphous phase) [30-33]. Owing to these advanced features, electrochemically self-doped TiO_2 NTAs (known as reduced-TiO_2 NTAs, *r*-TiO_2 NTAs) are currently considered among the most innovative materials in the areas of energy storage, electrolysis, and photolysis [34-44].

Nevertheless, in spite of remarkable research interest in *r*-TiO_2 NTAs, they have not been comprehensively reviewed. Therefore, in this study, we critically review an important aspect of *r*-TiO_2 NTAs, namely their synthesis and applications NTAs. Firstly, to provide a fundamental understating of *r*-TiO_2 NTAs, the fabrication and applications of pristine TiO_2 NTAs are briefly reviewed. Subsequently, recent findings on the major principles and mechanisms of electrochemical self-doping are discussed with theoretical and experimental evidence. Finally, we review the enhanced key functional features of *r*-TiO_2 NTAs and their applications and further propose possible directions for future research and highlight the challenges that are to be overcome.

†To whom correspondence should be addressed.
E-mail: jeyong@snu.ac.kr, choonsoo@kongju.ac.kr
‡These authors contributed equally to this work.

SYNTHESIS AND APPLICATIONS OF TiO_2 NANOTUBE ARRAYS

1. Synthesis of TiO_2 NTAs

After the first report on organized TiO_2 NTAs synthesized by anodization [45,46], Grimes and Schumuki's research has helped in advancing our understanding of highly self-aligned TiO_2 NTAs [1,8]. They precisely controlled the morphological features of TiO_2 NTAs, such as their length, pore size, and wall thickness [47-49] in addition to clearly elucidating the effects of electrolyte composition, pH, and applied potential on nanotube geometry [50-53]. In general, well-organized TiO_2 NTAs (as shown in Fig. 1(a)) are prepared by the anodization of a titanium (Ti) substrate at a constant voltage (in the range of 1-30 V in aqueous media and 5-150 V in organic media) in an electrolyte containing 0.1-1 wt% fluoride ions (F^-) [1]. Upon the application of a constant voltage, Ti is oxidized to $Ti^{(IV)}$, which can simultaneously form a compact TiO_2 layer with O^{2-} (from H_2O in the electrolyte) and soluble TiF_6^{2-} complexes (with F^- in the electrolyte) (Fig. 1(b)). Nanoporous structures in TiO_2 NTAs are established by a competition between oxide formation and complex dissolution; typical current-time profiles during anodization are displayed in Fig. 1(c).

Nanotube geometry is influenced by anodization voltage and time as well as by electrolyte conditions (Fig. 2(a)). Anodization voltage is a fundamental factor for controlling nanotube diameter [54,55], while tube length can be controlled by manipulating the anodization time [52,56]. Further, anodization conditions, such as electrolyte water content, conductivity, fluoride ion concentration, and pH, determine tube growth and ordering [53]. For example, a high water content in the electrolyte can cause ripples on nanotube surfaces due to a faster complex dissolution rate when compared to tube growth rate [57]. In addition, organic electrolytes allow the introduction of a carbon-rich phase in inner tubular layers due to electrolyte decomposition [26,58]. Electrolyte pH also affects the complex dissolution rate; anodization at a low pH results in a shorter tubular length when compared to anodization at a high pH [8]. These observations can be explained by the flow mechanism (Fig. 2(b)), according to which nanotube growth originates from (1) plasticity of the oxide layer via oxide volume expansion (Pilling-Bedworth ratio) and electrostrictive forces, and (2) migration of O^{2-} and F^- into inward oxide layer lattices to extend tube length [59-61].

2. Properties of TiO_2 NTAs

The crystal phase of TiO_2 NTAs is thought to be the primary factor determining their physical and chemical properties. In most of the cases, the crystal phase of anodized TiO_2 NTAs (as-prepared TiO_2 NTAs) is amorphous phase, apart from the nanotube formation at a high anodization voltage resulting in nanocrystallites in the tubes [1,8,62]. The amorphous phase is converted into anatase-

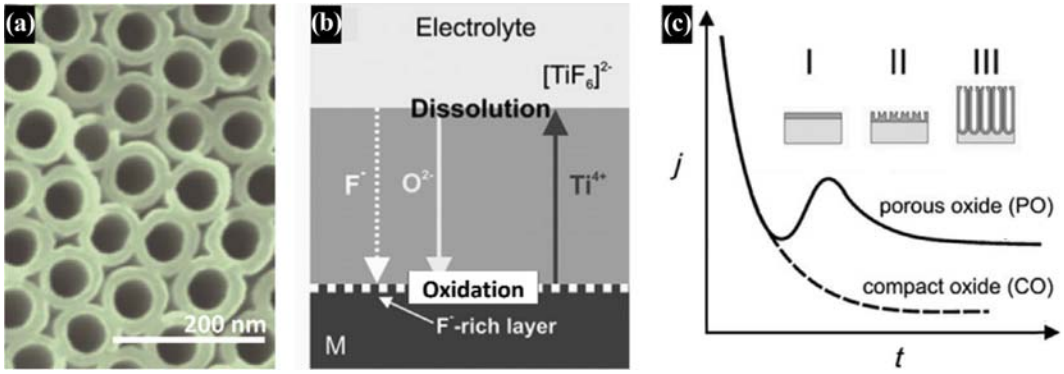

Fig. 1. (a) Morphology of TiO_2 nanotube arrays (NTAs) and (b) schematic illustration of ion transportation during nanotube formation in an electrolyte containing fluoride ion, and (c) typical current-time (j-t) profiles during electrochemical anodization for the fabrication of TiO_2 NTAs (reproduced with permission from Ref. [1]).

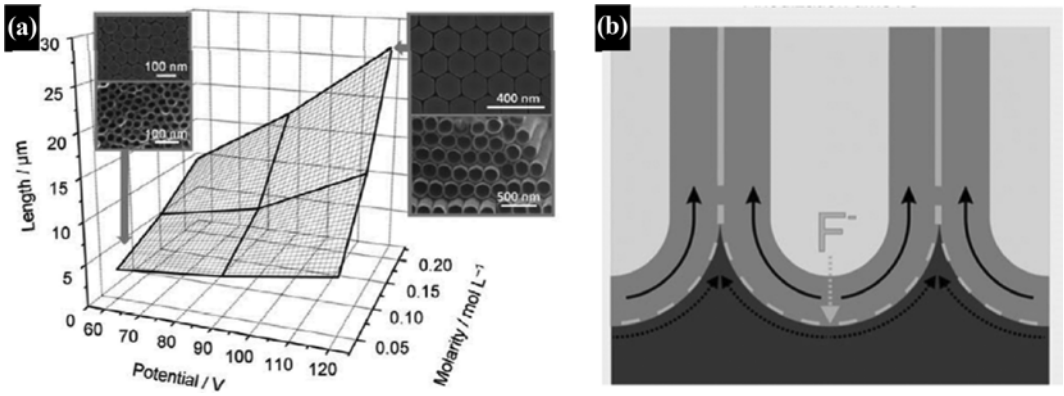

Fig. 2. (a) Correlation between anodization parameters and the geometrical aspects of TiO_2 NTAs and (b) flow mechanism interpreting the formation of nanotubes in TiO_2 NTAs (reproduced with permission from Ref. [1] and [53]).

and rutile-dominant crystalline structures upon thermal treatment (annealing) at 300-500 °C and over 550 °C in air, respectively [29]. During this transition, annealing conditions affect not only the transition temperature and phase ratio, but also the morphology and conductivity [8]. The existence of foreign elements leads to either a retarded or accelerated phase-transition process [63] and affects the transition temperature [64]. At a high annealing temperature, it is reported that TiO_2 NTAs exhibit unexpected cracks and collapsing in tubes [1]. Some cracks were observed at temperature above 450 °, possibly hindering electron transport. Additionally, when TiO_2-NTAs was fabricated in ethylene glycol, the nanotube structure was collapsed from 650 ° with the effect of ramping rate.

Depending on the crystal phase of TiO_2, the bandgap is approximately 3.2-3.5 eV for the amorphous phase, 3.2 eV for the anatase phase, and 3.0 eV for the rutile phase [65]. Particularly, the tubular structure of TiO_2 NTAs induces size quantization for below 12 nm of tube wall thickness, thus resulting in a highly complex band structure [66]. For instance, the bandgap of TiO_2 NTAs (anatase phase) is around 3.3 eV, which is slightly higher than the bandgap of anatase TiO_2 in the bulk phase (3.2 eV) [25].

In addition, annealing temperature influences the electrical conductivity of TiO_2 NTAs. Up to an annealing temperature of 200 °C, electrical conductivity decreases due to the evaporation of surface water. Meanwhile, conductivity increases drastically upon the transition of the amorphous phase into an anatase-dominant phase upon annealing at 300-500 °C. However, conversion into a rutile-dominant phase leads to a significant increase in resistivity at annealing temperatures greater than 500 °C [1]. Furthermore, annealing results in a number of surface defects on TiO_2 NTAs due to the production of oxygen vacancies and presence of $Ti^{(III)}$ [67]. This causes the formation of gas-adsorption sites, resulting in various reactions such as CO oxidation, selective reduction of nitrogen oxide species (NO_x), and H_2O decomposition [68,69].

With respect to electrochemical properties, a negatively biased potential enables TiO_2 NTAs to be colored by inserting small ions (protons, Li ions, etc.) into TiO_2 lattices [8], resulting in electrochromism [70]. During anodic polarization, carrier depletion occurs in TiO_2 NTAs, owing to which their electrocatalytic activity is extremely reduced for oxygen evolution and oxidant generation. Therefore, they are rarely used as anode materials by themselves [25], but are considered as substrates decorated with noble metal catalysts [71].

3. Applications of TiO_2 NTAs

Photolysis is the most critical application of TiO_2 NTAs in which charge carriers (i.e., holes and electrons) are generated by UV illumination [5]. Commonly, holes generated in the valence band diffuse to the surface of TiO_2 NTAs and produce hydroxyl radicals ($^{\bullet}OH$) when they react with adsorbed water molecules, while electrons induced in the conduction band trigger the formation of superoxide radicals($O_2^{\bullet-}$) upon reaction with oxygen molecules [72] (Fig. 3). Because holes and radicals are notably effective in a degradation of organic pollutants, these materials are being widely investigated for air cleaning, water purification, disinfection, and removal of residual pesticides from agricultural lands [73]. Furthermore, the induced electrons can lead to the evolution of hydrogen instead of superoxide radicals when the band-edge position of the conduction band is controlled via various doping methods [17]. In this

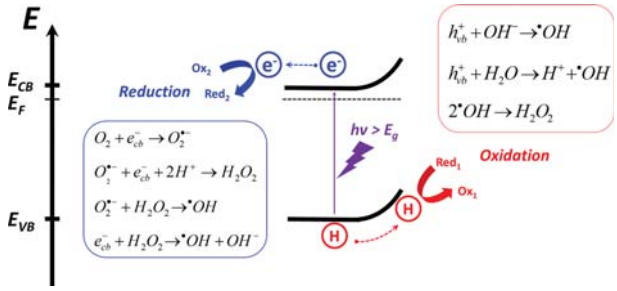

Fig. 3. Photolysis mechanism of TiO_2 NTAs with photo-generated holes and electrons; these induce various redox reactions on their surfaces. E_{CB}, E_F, and E_{VB} indicate energy levels of the conduction band, Fermi level, and valence band, respectively.

manner, there have been many research studies to improve the efficiency of solar energy conversion for hydrogen production by surface decoration with noble metal catalysts and hole-scavenger addition [1,17,74,75]. However, the bandgap of TiO_2 NTAs is too large to utilize visible light, which limits their photochemical applications to the UV regime [76]. Therefore, the bandgap structure of TiO_2 NTAs should be controlled for to effectively utilize visible light, which is a great challenge.

Dye-sensitized solar cells (DSSCs) are an attractive application of TiO_2 NTAs for energy harvesting by solar energy conversion [5]. In a DSSC with TiO_2 NTAs, the system utilizes a dye as a sensitizer attached onto TiO_2 NTA surfaces and organic solvents containing electron donors for the regeneration of photo-activated dyes. A typical DSSC operation consists of two steps - injection of electrons from photo-activated dyes into the conduction band of TiO_2 NTAs and regeneration of oxidized dyes with redox couples such as iodide/triiodide couples [77]. A high light-harvesting efficiency was found in nanotube-based DSSCs rather than in DSSCs incorporating nanoparticles. This can be attributed to the better light scattering, less recombination, and direct electron path of nanotubular structures [78,79].

Biomedical coatings and drug delivery are being considered as emerging applications of TiO_2 NTAs [8]. It is a very fascinating feature of TiO_2 NTAs that they can be simply synthesized with highly aligned and well-controlled nanotubular structures. Many studies successfully demonstrated the feasibility of TiO_2 NTAs for biomedical applications [1]. TiO_2 NTAs surface accelerates the formation of hydroxyapatite, which is a fundamental factor for growth of a biomedical implant for native bone [80]. The switchable photocatalytic reactions of TiO_2 NTA were also utilized for delivering a model drug at the target location and changing surface properties, which is essential for biomedical applications [81,82]. In addition, in the field of electrochromic devices and gas sensing, a number of approaches have been employed to take advantage of the electrochromic effect and surface reactivity of TiO_2 NTAs [83-85].

ELECTROCHEMICAL SELF-DOPED TiO_2 NANOTUBE ARRAYS

1. Electrochemical Self-doping

In spite of the many advantages and applications of TiO_2 NTAs,

their large bandgap must be a major challenge that needs to be overcome for future opportunities. Until now, there have been extensive investigations to control the band structure of TiO_2 NTAs. For instance, several foreign elements including metals (e.g., Co, Ni, Cr, Fe, and Nb) and non-metals (e.g., N, C, B, and F) have been introduced as promising dopants via various methods, including 1) thermal treatment with gas-phase dopants, 2) sputtering in an atmosphere containing dopants, 3) high-energy ion implantation, and 4) direct doping during anodization with suitable substrate alloys and incorporation of electroactive species [8,14]. However, complicated processes requiring high temperatures and pressures limit TiO_2 NTA applications.

Contrary to conventional doping with foreign impurities, electrochemical self-doping narrows the bandgap of TiO_2 NTAs in mild conditions. This methodology produces $Ti^{(III)}$ as a dopant by intercalation with small ions, particularly proton (H^+), upon cathodic polarization (Fig. 4(a)) [25]. Cathodic polarization causes the blue coloration of TiO_2 NTAs (Fig. 4(b)), which can be attributed to the electrochromic effect of transition metal oxides, such as TiO_2, WO_3, MnO_2, and Nb_2O_5 [86]. In the electrochromic phenomenon, proton intercalation is highly reversible and $Ti^{(III)}$ can be simply oxidized when an anodic biased potential is applied [70]. Intriguingly, TiO_2 NTAs distinctly show the irreversible feature, which is different with a previously reported reversible electrochromism. This observation is well supported by cyclic voltammetry (CV) measurements on pristine TiO_2 NTAs (anatase phase). As shown in Fig. 4(c), prior to cathodic polarization, electrocatalytic activity was not observed for pristine TiO_2 NTAs for the oxygen evolution reaction (OER) in the potential range of 0-3.0 V (potential regime I). At a negatively biased potential of approximately −0.7 V (vs. Ag/AgCl) (potential regime II), cathodic polarization leads to proton intercalation with coloration of pristine TiO_2 NTAs ranging from gray to blue, which implies the fabrication of *r*-TiO_2 NTAs (blue TiO_2 NTAs) [33]. After cathodic polarization in the 1st cycle, CV curves of *r*-TiO_2 NTAs during the 2nd and 3rd cycles show an irreversible conversion when compared to the CV curve of the 1st cycle; this can be attributed to the strongly negative potential applied (below −1.0 V vs. Ag/AgCl) (indeed, applying a negative potential in the range of −0.7 to −1.0 V (vs. Ag/AgCl) for cathodic polarization triggers a reversible electrochromic effect). This eventually results in the formation of oxygen vacancies by the cleavage of Ti-O bonds in TiO_2 lattices [87], and they are evidently different from those in pristine

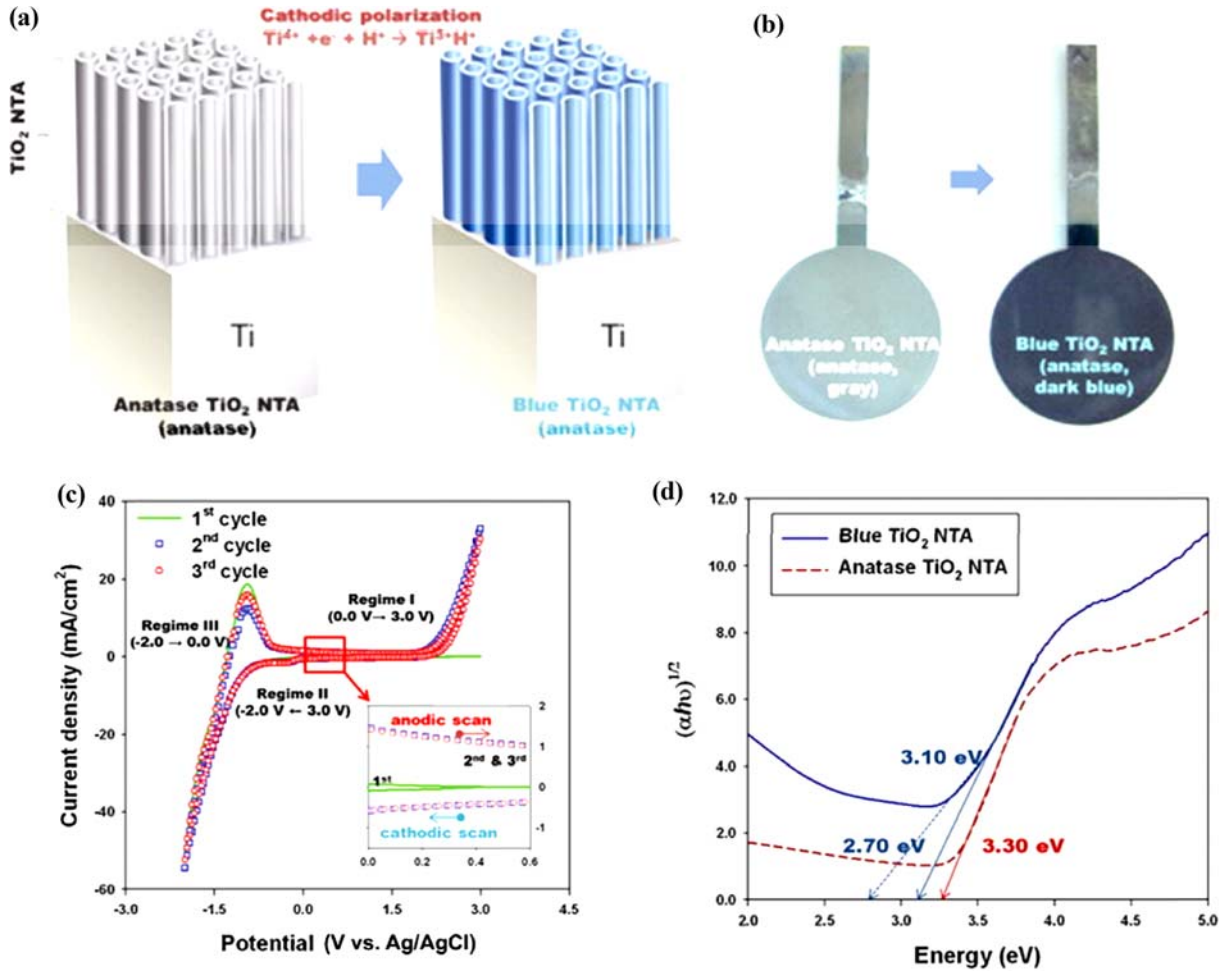

Fig. 4. (a) Schematic illustration of electrochemical self-doping of TiO_2 NTAs. (b) A photograph of TiO_2 NTAs before and after electrochemical self-doping, (c) effects of doping examined by cyclic voltammetry, and (d) electronic properties of *r*-TiO_2 NTAs (blue TiO_2 NTAs) and pristine TiO_2 NTAs (anatase phase) (reproduced with permission from Ref. [25]).

TiO_2 NTAs. Significant enhancement in the capacitive and electrocatalytic activity for OER is observed in the potential range of 0 to 0.6 V (inset of Fig. 4(c)) and above 2.0 V. Electronic states were examined by diffuse reflectance UV-vis absorption spectroscopy (Tauc plots) (Fig. 4(d)), and the enhancement in these activities was attributed to bandgap narrowing by cathodic polarization [19,27, 88-90]. Consequently, it can be rationalized that pristine TiO_2 NTAs are irreversibly doped by cathodic polarization [26] and electrochemical self-doping is a simple and practical method for controlling the electronic properties of TiO_2 NTAs.

2. Principle of Electrochemical Self-doping

$Ti^{(III)}$ produced in the TiO_2 lattice plays a fundamental role as the self-dopant in the electrochemical self-doping process. The presence of $Ti^{(III)}$ could be clearly elucidated by analyzing X-ray photoelectron spectroscopy (XPS) patterns and is supported by a reduction mechanism (Fig. 5) [26,29,31,32,87,88,91]. Compared to Ti $2p_{1/2}$ and Ti $2p_{3/2}$ peaks of $Ti^{(IV)}$ for pristine TiO_2 NTAs in Ti 2p XPS spectra at around binding energy of 458.9 and 464.2 eV (Fig. 5(a)), those of *r*-TiO_2 NTAs are negatively shifted [15,92]. Such characteristic shifts in Ti $2p_{1/2}$ and Ti $2p_{3/2}$ peaks evidently suggest the production of $Ti^{(III)}$ during electrochemical self-doping. In addition, oxygen in the TiO_2 lattice (Fig. 5(b)) is associated with two split peaks, including lattice oxygen in Ti-O-Ti bonds at 529.8 eV and surface oxygen in Ti-OH bonds at 531.5 eV. After electrochemical self-doping, the peak corresponding to surface oxygen obviously intensified due to the formation of surface hydroxyl groups [41,93]. Nevertheless, discussion on whether hydroxyl groups are formed or not by electrochemical self-doping is still ongoing [25,32,87]. The mechanism of electrochemical self-doping can be interpreted as a combination of the conventional energy-band model and chemical evolution of the basic building blocks of TiO_2 [32]. According to the energy-band model (Fig. 5(c)), cathodic polarization injects electrons into the conduction band as photo-excited electrons, leading to oxygen vacancies with the reduction of $Ti^{(IV)}$ to $Ti^{(III)}$ in TiO_6^{2-} octahedrons to form Ti-O-Ti bonds. Charge neutrality in these octahedrons is unbalanced due to oxygen vacancies and it is later compensated by proton insertion in adjacent TiO_6^{2-} octahedrons ($Ti^{(IV)}O_2+H^++e^-\rightarrow Ti^{(III)}O(OH)$) [91]. With the formation of $Ti^{(III)}$, the insulating surfaces of pristine TiO_2 NTAs are converted into highly conductive surfaces, which occurs from bottom to whole internal surface of nanotube structure.

In electrochemical self-doping, various parameters, such as strong negative potential for cathodic polarization and crystal structure, have an effect on the formation of $Ti^{(III)}$. Zhou and Zhang [87] reported that a low negative potential of −0.5 V (vs. Ag/AgCl) is insufficient to reduce $Ti^{(IV)}$ to $Ti^{(III)}$, which results in a reversible conversion that can be utilized in electrochromic devices. A potential below −2.0 V (vs. Ag/AgCl) leads to nanotube destruction. This suggests that a negative potential of a certain magnitude should be applied for successful electrochemical self-doping [41,94]. Moreover, Kim and co-workers [29] demonstrated the effect of crystal structures of TiO_2 NTAs on electrochemical self-doping. They showed that the anatase phase in TiO_2 lattice is more favorable than the rutile phase, as the former has better structural stability for H^+ accommodation during electrochemical self-doping.

In addition, according to synthesis protocols based on the crys-

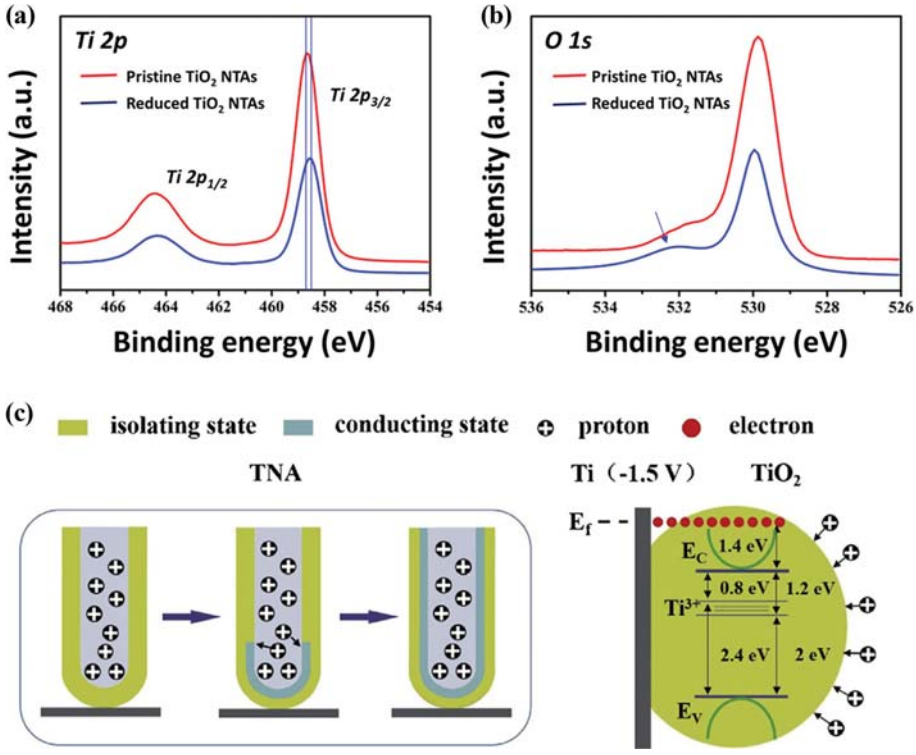

Fig. 5. High-resolution XPS spectra of (A) Ti 2p and (B) O 1s in pristine and *r*-TiO_2 NTAs, and (C) Energy-band model for the interpretation of $Ti^{(III)}$ formation in Ti-TiO_2 heterojunctions by cathodic polarization (reproduced with permission from Ref. [32] and [93]). Please note that TNA in (C) indicates TiO_2 nanotube array which is same with TiO_2 NTAs.

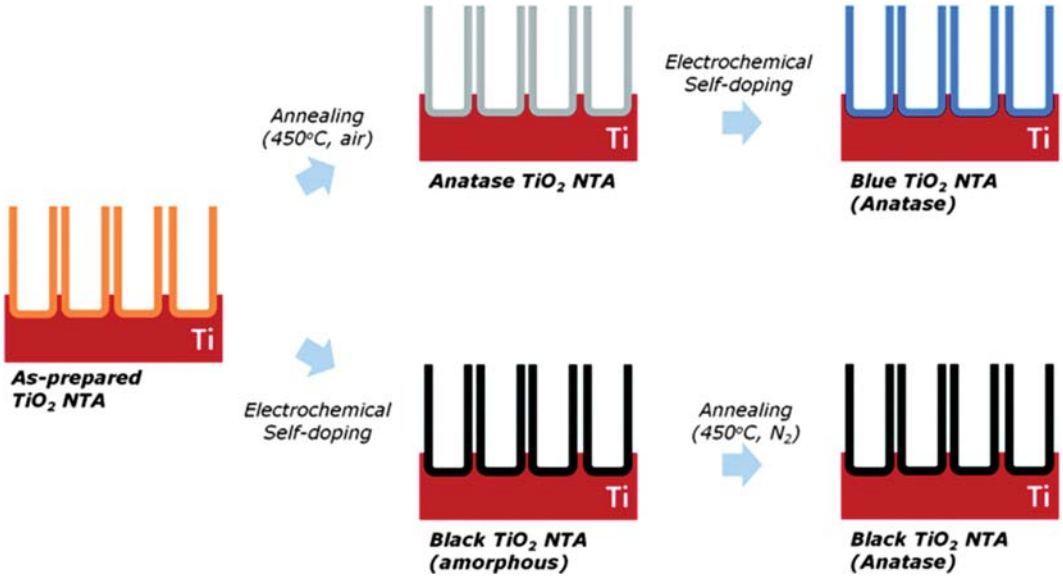

Fig. 6. Schematic of the fabrication of blue and black colored TiO_2 NTAs by electrochemical self-doping (reproduced with permission from Ref. [31]).

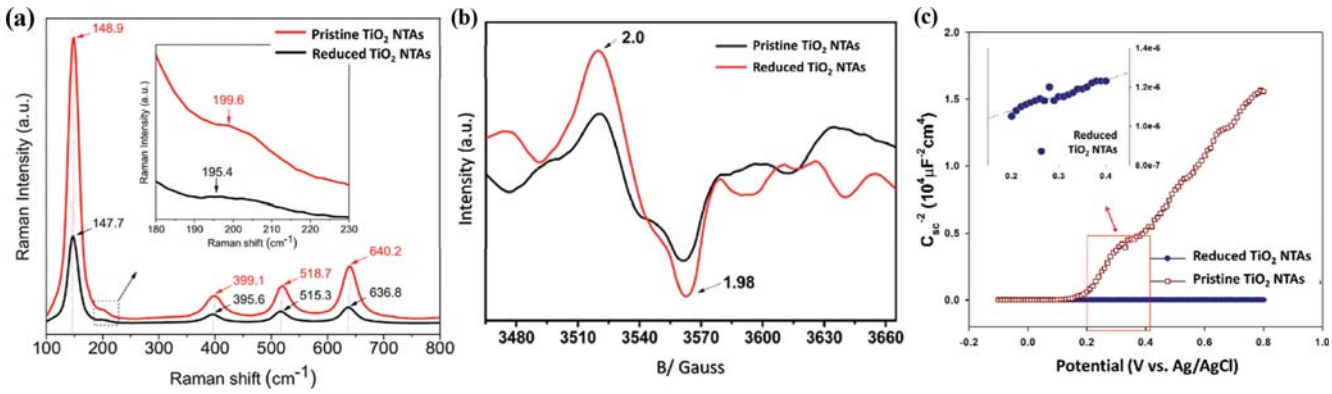

Fig. 7. (a) Raman spectra, (b) EPR spectra, and (c) Mott-Schottky plots of pristine and electrochemically self-doped (reduced) TiO_2 NTAs (reproduced with permission from Ref. [26, 27]and [91]).

tal structures of TiO_2 NTAs (Fig. 6) [31], two classes of *r*-TiO_2 NTAs can be defined: blue and black TiO_2 NTAs. As shown in Fig. 6, blue TiO_2 NTAs are fabricated by the electrochemical self-doping of pristine TiO_2 NTAs with the anatase phase while black TiO_2 NTAs are prepared by the electrochemical self-doping of as-prepared TiO_2 NTAs with the amorphous phase or thermally treated TiO_2 NTAs (reported as red-colored TiO_2 NTAs) at low temperatures under atmospheric conditions (which leads to enhanced mechanical stability); this process is followed by annealing under inert conditions. In general, black TiO_2 NTAs can be synthesized only by the doping of amorphous TiO_2 NTAs and they exhibit slightly higher levels of doping as compared to blue TiO_2 NTAs. This is because the amorphous phase of TiO_2 NTAs contains larger spatial channels with disordered structures and defects for proton intercalation during electrochemical self-doping when compared to the anatase phase [26]. Besides, additional carbon doping is thought to increase dopant level in black TiO_2 NTAs; this additional carbon originates from residual ethylene glycol as the carbonaceous precursor during annealing under inert gas conditions [58].

The presence of $Ti^{(III)}$ is further demonstrated by Raman and electro paramagnetic resonance (EPR) spectra (Fig. 7). In their Raman spectra (Fig. 7(a)), pristine and *r*-TiO_2 NTAs exhibit four distinct peaks corresponding to the E_g, B_{1g}, A_{1g}/B_{1g}, and E_g modes at approximately 147, 395, 516, and 640 cm^{-1}, respectively. These are related to symmetric stretching vibrations (E_g), bending vibrations (B_{1g}), and anti-symmetric bending vibrations (A_{1g}/B_{1g}) in Ti-O-Ti bonds [91]. Upon electrochemical self-doping, peak broadening and a blue shift are observed for the E_g mode, which is sensitive to oxygen vacancies in TiO_2 [95]. In particular, although peak position and shape are influenced by several factors, including phonon confinement, non-homogeneity of particle size, and non-stoichiometric lattice defects, the effect of these factors is negligible in the Raman spectra of TiO_2 NTAs electrochemically doped by cathodic polarization [96]. Furthermore, $Ti^{(III)}$ induced by electrochemical self-doping can also be verified by EPR spectra (Fig. 7(b)). A strong signal is observed in the EPR spectrum of *r*-TiO_2 NTAs at g val-

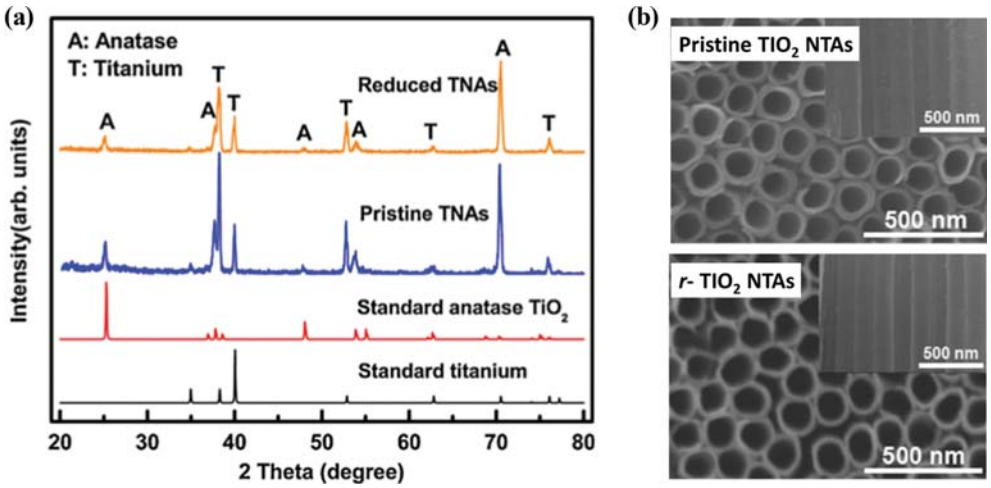

Fig. 8. (a) XRD patterns and (b) SEM images of pristine and *r*-TiO_2 NTAs. The XRD patterns were indexed to the JCPDS file of standard titanium (PDF 65-6231) and anatase TiO_2 (PDF 21-1272) (reproduced with permission from Ref. [88] and [98]). Please note that TNAs in (a) indicates TiO_2 nanotube array which is same with TiO_2 NTAs.

ues of 2.004 and 1.994, corresponding to $Ti^{(III)}$ and oxygen vacancies, respectively [93,97]. From XPS, Raman, and EPR analyses, it could be clearly confirmed that electrochemical self-doping allows the formation of $Ti^{(III)}$. This results in a drastic increase in the charge carrier density (level of dopant), which can be realized from the inverse slope of the Mott-Schottky plot (Fig. 7(c)). The high level of dopant with $Ti^{(III)}$ formation plays a critical role in enhancing the electrochemical, photocatalytic, and optical properties of TiO_2 NTAs [26].

However, the formation of $Ti^{(III)}$ in TiO_2 NTAs seldom affects the crystal structure and surface morphology of TiO_2 NTAs (Fig. 8). In the XRD patterns (Fig. 8(a)), the peak positions of *r*-TiO_2 NTAs mostly agree with those of pristine TiO_2 NTAs, implying no noticeable transformation in the crystal structure due to electrochemical self-doping [25,96]. Although electrochemical self-doping causes a reduction in the average crystallite size of TiO_2 NTAs, which can be estimated by applying the Scherrer equation to analyze XRD patterns, it is also not remarkable. Additionally, the nanotubular structure of *r*-TiO_2 NTAs is identical to that of pristine TiO_2 NTAs (Fig. 8(b)). This suggests that the formation of $Ti^{(III)}$ by electrochemical self-doping causes no damages in the crystal structure and morphology [25,26,29,31,87,96].

KEY FUNCTIONAL FEATURES OF *r*-TiO_2 NTAS

1. Capacitive Properties of r-TiO_2 NTAs

Compared to bare TiO_2, TiO_2 NTAs are widely believed to have better capacitive properties due to their structural features, including a high surface area, interconnectivity of active materials, good contact with the Ti substrate, and well-organized perpendicular nanostructures [1,8,99]. These structural advantages offer a direct pathway to electron transfer, thus improving conductivity, when compared to TiO_2 nanoparticle structures due to the disordered pathway provided by interparticle connections between non-oriented TiO_2 (nano particles). Moreover, open-end nano channels provide a high ionic mass transfer with easy accessibility to solvated ions. Therefore, TiO_2 NTAs are considered promising electrode materials for electrochemical supercapacitors [15,99]. Electrochemical self-doping can further improve the potential of TiO_2 NTAs as supercapacitors with geometrical advantages. Due to the high level of doping induced by electrochemical self-doping, *r*-TiO_2 NTAs exhibit highly enhanced capacitive properties (Fig. 9) [26]. A nearly rectangular shape is observed in the corresponding CVs with a significantly enhanced plateau current for *r*-TiO_2 NTAs when compared to pristine TiO_2 NTAs; this indicates their superior electrical double layer capacitor (EDLC)-like properties (Fig. 9(a)). Furthermore, their areal capacitances were estimated to be 15-24 mF/cm^2 at a scan rate of 0.08-100 mV/s, which are remarkably higher than those of pristine TiO_2 NTAs (*ca.* 0.05-0.1 mF/cm^2) (Table 1) [24]. In direct comparison with *r*-TiO_2 NTAs (blue and black TiO_2 NTAs), black TiO_2 NTAs show an areal capacitance two-times greater than that of blue TiO_2 NTAs [31].

Note that *r*-TiO_2 NTAs exhibit high rate capability and long-term service stability [32,33,91,96,102]. The areal capacitance of *r*-TiO_2 NTAs is maintained even at fast scan rates (or discharging rates) as shown in Fig. 9(b).

According to previous reports [26], areal capacitance values were maintained up to over 50% at fast scan rate of 1,000 mV/s compared to slow scan rate of 10 mV/s. Furthermore, only around 4% of reduction in retention performance during 5000 cycles indicates a high power density and stability [34].

The notable capacitive properties of *r*-TiO_2 NTAs were further supported by Nyquist plots and complex capacitance measurements in electrochemical impedance spectroscopy (EIS) [26,32,33]. In the Nyquist plots (Fig. 9(c)), a vertical line is observed in the low frequency region (the inset of panel C) for *r*-TiO_2 NTAs, while a 45° impedance line and depressed semicircular arc were found for pristine TiO_2 NTAs; this is a typical Nyquist plot for pristine TiO_2 NTAs, as observed from the transmission line model [87]. These results suggest superior capacitive properties for *r*-TiO_2 NTAs. The large integrated area of the complex capacitance curve and peak positions in its high-frequency region (Fig. 9(d)) indicate a large

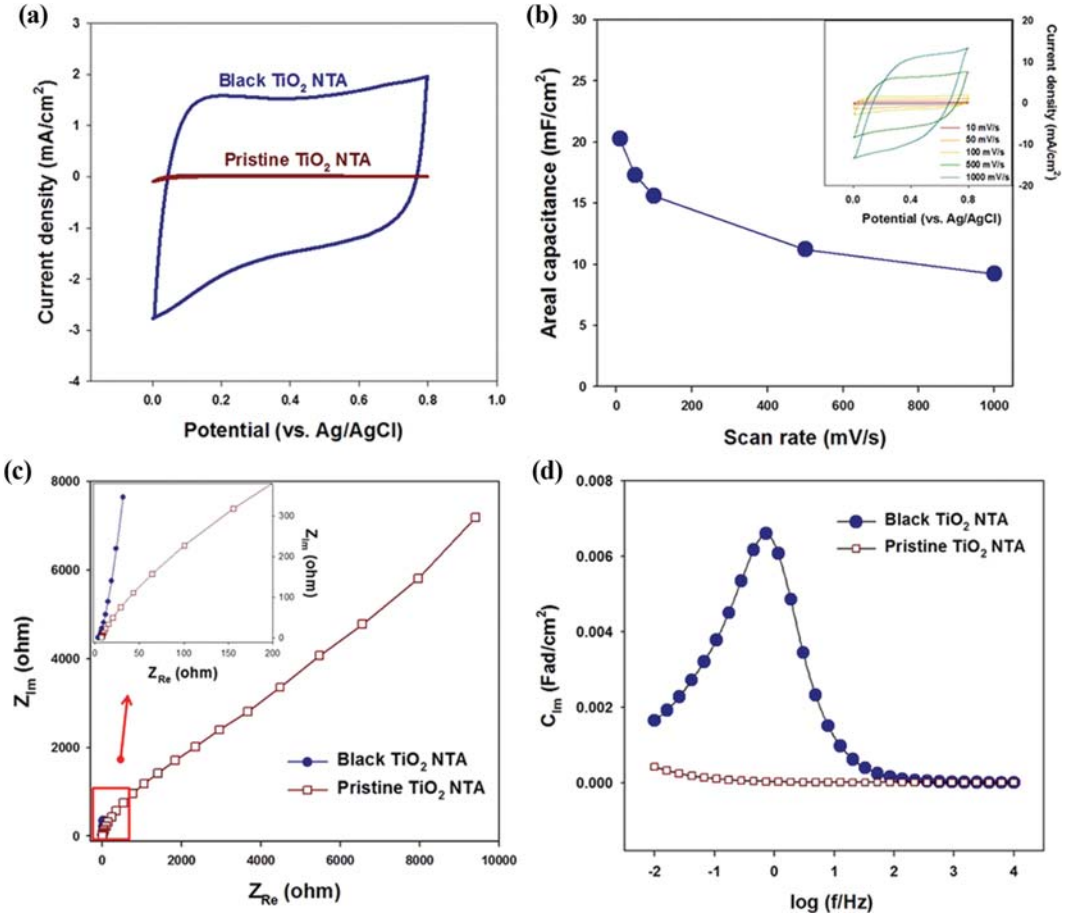

Fig. 9. Capacitive properties examined by (a) cyclic voltammetry, (b) areal capacitance measurements, (c) Nyquist plots, and (d) complex capacitances of pristine and *r*-TiO_2 NTAs (black TiO_2 NTAs) (reproduced with permission from Ref. [26]).

Table 1. Capacitance of pristine TiO_2 NTAs and *r*-TiO_2 NTAs

	Areal capacitance (mF/cm^2)	Scan rate (mV/s)	Ref.
TiO_2 nanoparticles	0.03-0.18	100-1	[99]
Pristine TiO_2 NTAs	0.08-2.4	100-50	[15,100]
r-TiO_2 NTAs (blue)	6.5-20.05	100-50	[24,35,91,101]
	12-20.08	1-0.05 mA/cm^2 (Discharging rate)	[32,96]
r-TiO_2 NTAs (black)	15.6	100	[26]

double-layer capacitance and fast rate capability for *r*-TiO_2 NTAs.

Many studies have successfully demonstrated the capacitive properties of *r*-TiO_2 NTAs [24,33-35,91,102,104]; in addition, modification via decoration with metal oxides and carbon materials opens up further opportunities for *r*-TiO_2 NTA application in energy-storage devices such as pseudocapacitors and lithium-ion batteries [36,101,103,105-108]. For example, polypyrrole was coated on *r*-TiO_2 NTAs by electrochemical deposition [101], resulting in a significantly high specific capacitance of ~897 F/g at a specific current of 0.5 A/g and potential of −0.2 to 0.4 V (vs. Ag/AgCl). With the deposition of manganese oxide (MnO_2) via sequential chemical bath deposition [105], the areal capacitance of *r*-TiO_2 NTAs increased to 175 mF/cm^2. Furthermore, the capacitive properties of *r*-TiO_2 NTAs improved upon decoration with copper oxide (CuO_2) nanoparticles, as evidenced by square wave voltammetry measurements (specific capacitance of ~200 F/g at 0.2 A/g in the potential range of −0.6 to 0.3 V (vs. Ag/AgCl)) [106]. The applicability of *r*-TiO_2 NTAs as anodes in lithium-ion batteries has also been investigated (Fig. 10). Their specific capacity was estimated to be 333 mAh/g with a high rate performance and cycle stability, which is approximately 97% of the theoretical capacity (*ca.* 337 mAh/g) [103]. Coating with poly(phenylene oxide) on *r*-TiO_2 NTAs induces a significant enhancement in specific capacity (~500 mAh/g), which is required for their application in lithium-ion batteries [36,103, 107,108].

2. Electrocatalytic Properties of *r*-TiO_2 NTAs

Electrode materials for oxidant generation (e.g., chlorine (Cl_2), hydroxyl radicals ($^{\bullet}OH$), ozone (O_3), and hydrogen peroxide (H_2O_2))

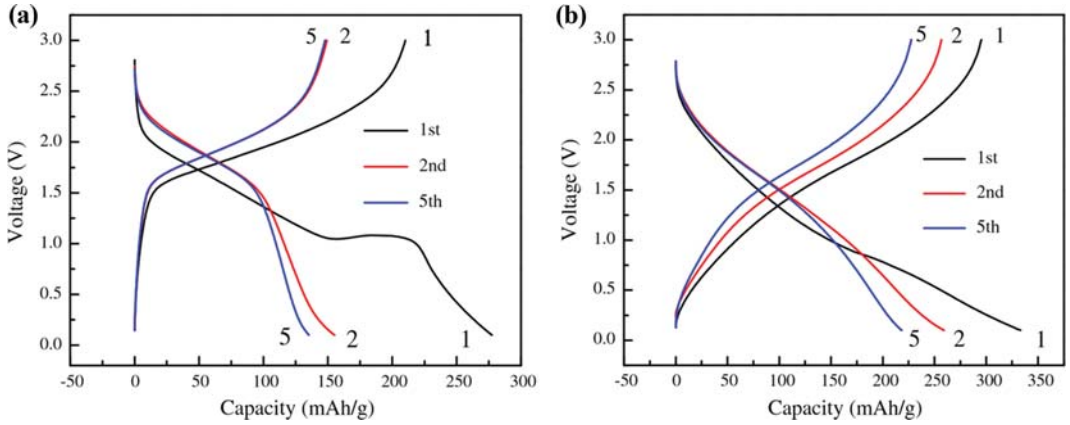

Fig. 10. Charging/discharging curves of (a) pristine TiO_2 NTAs and (b) *r*-TiO_2 NTAs (reproduced with permission from Ref. [103]).

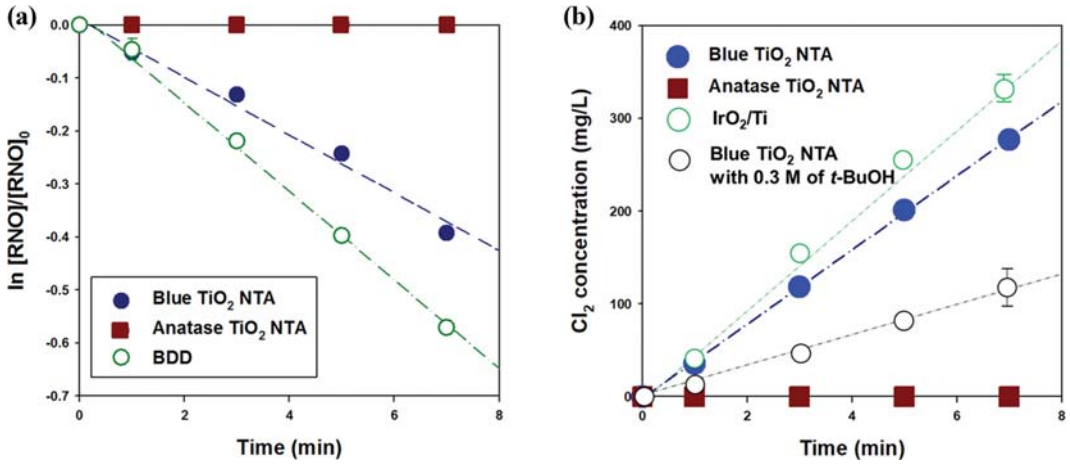

Fig. 11. Production of (a) hydroxyl radicals (•OH) and (b) chlorine (Cl_2) on *r*-TiO_2 NTAs (blue TiO_2 NTAs) as compared to their production on commercial boron-doped diamond electrodes (BDDs) and IrO_2/Ti (reproduced with permission from Ref. [25]).

play a critical role in many applications, including chlor-alkali processes, plastic manufacturing, pharmaceutical industry, and water treatment [109]. In the development of oxidant-generating electrodes, there have been two great technological and scientific breakthroughs in industrial electrochemistry, i.e., the introduction of dimensionally stable anodes (DSA) and boron-doped diamond electrodes (BDD), which are well-known anodes with high electrocatalytic activity for the production of Cl_2 and •OH, respectively [110, 111]. Nevertheless, their high synthesis costs led to a strong demand for novel electrocatalysts with high performance and low cost. Under these conditions, *r*-TiO_2 NTAs are suitable and promising electrode materials for oxidant generation.

The electrocatalytic activity of *r*-TiO_2 NTAs was extensively investigated by Kim and co-workers [25,26,29,31]. *r*-TiO_2 NTAs exhibit higher electrocatalytic activity for the OER when compared to pristine TiO_2 NTAs (Fig. 4(c)). From OER analysis of anodic-polarized current-potential profiles [31], the overpotential of *r*-TiO_2 NTAs was estimated to be greater than 1.0 V with respect to OER onset potential in neutral pH conditions (E_{OER}=0.608 V vs. Ag/AgCl at pH=7.2). The slope of the Tafel plot was approximately 200 to 400 mV/dec, implying that OER on *r*-TiO_2 NTAs is mediated by •OH. The production of •OH and Cl_2 was demonstrated using a colorimetric method based on *p*-nitrosodimetylaniline (RNO) bleaching and N,N-diethyl-*p*-penylenediamine (DPD) method, respectively (Fig. 11) [25,26]. From the semi-log plot shown in Fig. 11(a), it can be inferred that the production efficiency of •OH on *r*-TiO_2 NTAs was significantly higher than that on pristine TiO_2 NTAs. This result is comparable to that of BDD, which is a well-known anode for •OH production. In the case of Cl_2 evolution (Fig. 11(b)), a large amount of Cl_2 was electrochemically generated on *r*-TiO_2 NTAs but not on pristine TiO_2 NTAs. Moreover, the evolution of Cl_2 on *r*-TiO_2 NTAs was very similar to that on commercial IrO_2/Ti as DSA, suggesting their superior electrocatalytic activity for oxidant generation. In particular, the mechanism of Cl_2 evolution was elucidated by the addition of *t*-BuOH as a scavenger of •OH. The addition of *t*-BuOH partially inhibited the production of Cl_2 on *r*-TiO_2 NTAs. This implies that •OH plays a critical role in the production of oxidants on *r*-TiO_2 NTAs and •OH can be easily released from *r*-TIO_2 NTA surface into the bulk solution [25].

After discovering the good electrocatalytic activity of *r*-TiO_2 NTAs for oxidant generation, many studies attempted to improve their electrocatalytic activity for wastewater treatment, desalination, dis-

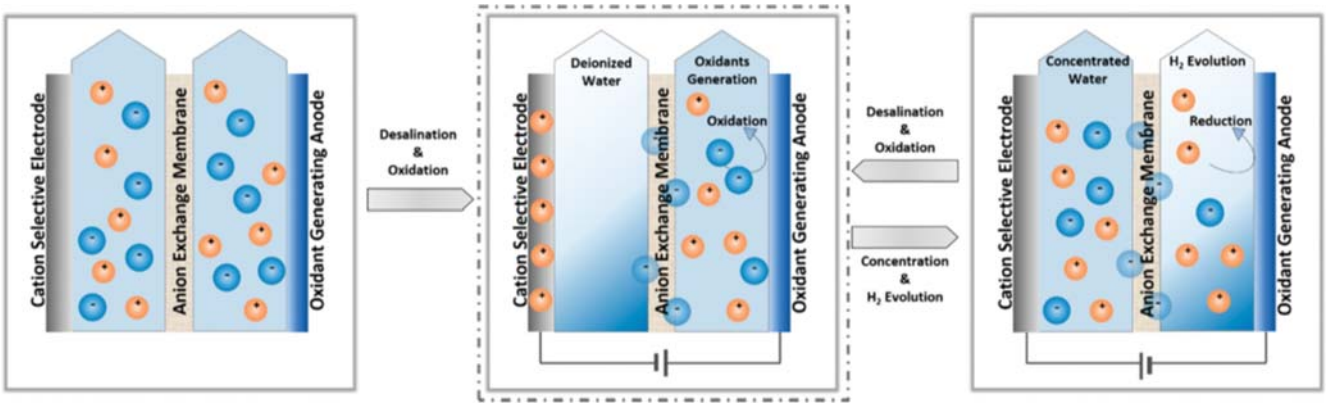

Fig. 12. Schematic illustration of a novel hybrid desalination system synchronized with oxidation and reduction processes using *r*-TiO_2 NTAs (reproduced with permission from Ref. [39]).

infection, and electrolysis for oxygen evolution and reduction [38, 39,112-118]. The electrochemical production of peroxodisulfate ($S_2O_8^{2-}$) on *r*-TiO_2 NTAs was proved by mechanistic investigations; peroxodisulfate is widely used as a strong oxidant in wastewater treatment and polymerization [38]. *r*-TiO_2 NTAs exhibit a high electrochemical performance for the removal of chemical oxygen demand (COD), NH^{4+}, and total organic carbon (TOC) with low energy consumption in wastewater treatment [113,114]. In the case of electrochemical disinfection [115], the high effectiveness of *r*-TiO_2 NTAs was demonstrated by *E. coli* inactivation in real wastewater matrices. With modification by coating and doping with metals and metal oxides, such as Au, Co, RuO_2, and IrO_2 [112,114, 116,118], their electrocatalytic activity for the production of Cl_2 and oxygen evolution and reduction could be drastically improved. Moreover, *r*-TiO_2 NTAs were demonstrated as promising electrode materials for oxidants generation in the hybrid desalination system of desalination and oxidation (Fig. 12). They work as anion and cation sinks with Cl_2 and H_2 production during desalting and concentrating processes, respectively. In this hybrid system, using *r*-TiO_2 NTAs opens up a new route for electrochemical desalination synchronized with water treatment and renewable energy storage with the production of Cl_2 and H_2.

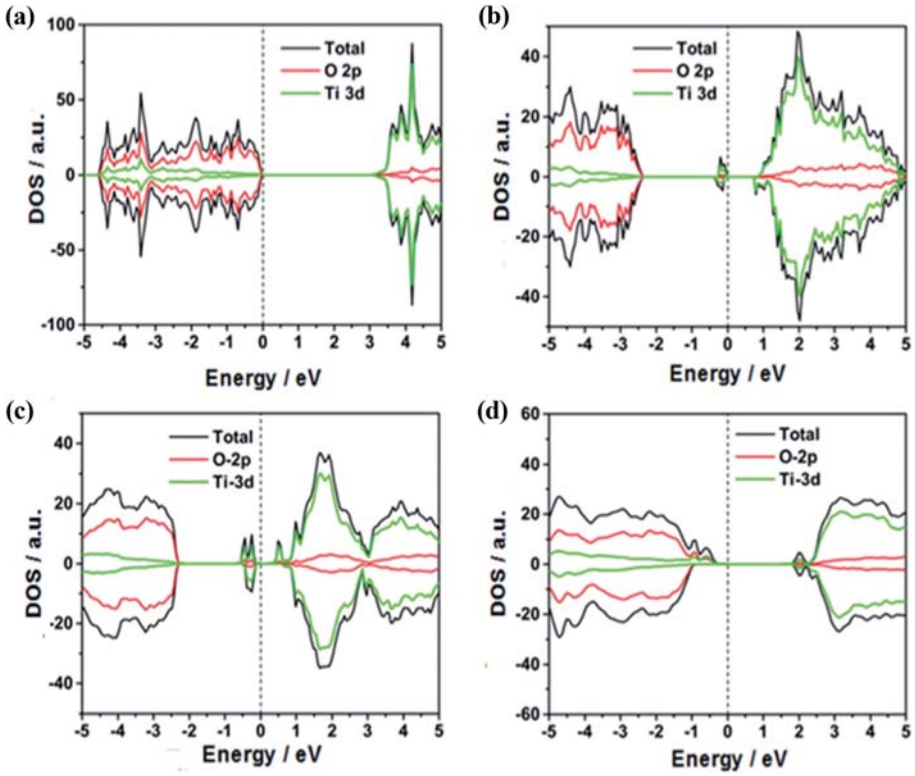

Fig. 13. Density of states (DOS) of (a) pristine TiO_2 NTAs and *r*-TiO_2 NTAs with (b) one, (c) two, and (d) three oxygen vacancies. The vertical dashed lines at zero indicate the Fermi level (reproduced with permission from Ref. [27]).

3. Photocatalytic Properties of *r*-TiO_2 NTAs

Finding strategies to synthesize highly effective TiO_2 NTAs for photolysis systems is a challenge for energy and environmental applications [5]. Currently, *r*-TiO_2 NTAs are being considered as good alternatives for doped TiO_2 NTAs produced with foreign impurities, as their photocatalytic activity can be manipulated via a simple control over the band structure [1]. It was verified by experimental and computational studies that oxygen vacancies formed by electrochemical self-doping affect the band structure of *r*-TiO_2 NTAs [27]. In Fig. 13, compared to the band structure of pristine TiO_2 NTAs, oxygen vacancies produced during electrochemical self-doping give rise to localized $Ti^{(III)}$ in the near Fermi level [32,119]. This may play a role as a shallow donor level, resulting in the easy separation of photo-generated holes and electrons and a shift in the Fermi level to the conduction band (Fig. 13(a) and (b)). However, when excess $Ti^{(III)}$ sites are induced by two oxygen vacancies, recombination of photo-generated holes and electron is facilitated because excess $Ti^{(III)}$ acts as trap sites for charge carriers. Furthermore, three oxygen vacancies cause the disappearance of $Ti^{(III)}$ states, which suggests the existence of an optimal doping concentration for the synthesis of *r*-TiO_2 NTAs.

Owing to the controlled band structure of *r*-TiO_2 NTAs, they exhibit a significantly enhanced photocatalytic activity [19,20,27, 28,40-42,89,90,93,98,119-121]. Zhang and co-workers reported a high performance for *r*-TiO_2 NTAs in terms of the photocurrent density (2.8 mA/cm^2) at 1.23 V vs. a reversible hydrogen electrode (RHE) and a photo conversion efficiency of 1.27% in solar-driven water-splitting systems [19]. A number of studies demonstrated the superiority of *r*-TiO_2 NTAs as photoelectrodes for solar water splitting in terms of their dependence on applied potential and reduction time during electrochemical self-doping, modification; these claims were further supported by theoretical evidence [41,90,98]. According to a previous study [98], a mixed anatase and rutile phase is preferred for enhanced photocatalytic activity instead of a single crystal phase as the mixed phase exhibits a synergistic effect and produces a large number of oxygen vacancies. Density functional theory (DFT) calculations offer new insights into the surface state of *r*-TiO_2 NTAs in terms of charge separation, transfer, and injection in the water-splitting reaction [41]. By modifying *r*-TiO_2 NTAs, their photocatalytic activity could be improved [119,120].

The high photocatalytic activity of *r*-TiO_2 NTAs has led to numerous studies on their application for wastewater treatment [20,28, 122]. Under illumination with simulated sunlight, *r*-TiO_2 NTAs exhibit a much higher photocatalytic performance with a large photocurrent, an accelerated OER, and iodide and urea degradation when compared to pristine TiO_2 NTAs [28]. The visible-light activity of *r*-TiO_2 NTAs was demonstrated by a Rhodamine B and phenol oxidation reaction and *E. coli* inactivation [20]. From the practical point of view [122], *r*-TiO_2 NTAs provide opportunities to overcome the major limitations faced by heterogeneous photocatalysts: 1) no additional separation step is required to reuse the photocatalyst and clarification effluent, 2) the immobilized surface of *r*-TiO_2 NTAs rarely hinders the diffusion of reactants due to the geometrical features of *r*-TiO_2 NTAs with open porous tubes directly grown on the Ti substrate, 3) the photocatalytic activity of *r*-TiO_2 NTAs can be enhanced by designing photochemical systems to degrade organic pollutants and simultaneously produce H_2 as renewable energy (Fig. 14), and 4) *r*-TiO_2 NTAs enable photoelectrochemical system operation at low energies owing to which they can be operated without a power grid system.

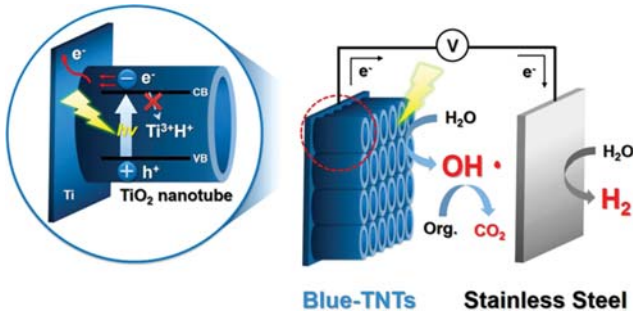

Fig. 14. Scheme of a photoelectrochemical system with *r*-TiO_2 NTAs for the degradation of organic compounds and H_2 production (reproduced with permission from Ref. [122]). Please note that Blue-TNTs indicate blue colored TiO_2 nanotubes which is same with r-TiO_2 NTAs (especially, blue colored TiO_2 NTAs).

FUTURE RESEARCH DIRECTIONS

One of the biggest challenges in this area is that there are no standardized metrics to evaluate the performance of *r*-TiO_2 NTAs owing to which it is difficult to compare their capacity, rate capability, electrocatalytic activity, electrocatalytic stability, and faradaic efficiency. Therefore, standard metrics benchmarked by energy storage devices, heterogeneous electrocatalysts, and solar water-splitting devices should be clearly designed with test protocols for active surface area, aspect ratio, current density, level of dopants, and light illumination.

Another challenge is the need to confirm the capability of *r*-TiO_2 NTAs as anodes by conducting investigations on various organic pollutants and pathogens. In addition, it should be determined whether the production of toxic byproducts from *r*-TiO_2 NTAs can be controlled during the electrochemical treatment of real water samples using bench-scale tests. Another point is that the long-term performance evaluation methodology for wastewater treatment remains unclear, and this should be resolved in future work. Furthermore, there are many complexities in fabricating and installing *r*-TiO_2 NTA-based devices owing to their poor mechanical stability, which can be attributed to a low adhesion between the tubular layer and substrate, leading to restricted flexibility, shape and thickness. The limited flexibility of *r*-TiO_2 NTAs also results in a low photoconversion efficiency in photocatalyst applications. Therefore, to expand the successful application of *r*-TiO_2 NTAs into research areas such as sensors, membranes, and biomaterials, the aforementioned key issues should be addressed.

ACKNOWLEDGEMENT

This was supported by the research grant of the Kongju National University in 2019, and by the research grant of the Waste to Energy Recycling Human Resource Development Project of Korea Minis-

try of Environment (ME).

REFERENCES

1. P. Roy, S. Berger and P. Schmuki, *Angew. Chem. Int. Ed.*, **50**, 2904 (2011).
2. G. K. Mor, K. Shankar, M. Paulose, O. K. Varghese and C. A. Grimes, *Nano Lett.*, **6**, 215 (2006).
3. Y. Hou, X. Li, Q. Zhao, X. Quan and G. Chen, *Environ. Sci. Technol.*, **44**, 5098 (2010).
4. Y. Jun, J. H. Park and M. G. Kang, *Chem. Commun.*, **48**, 6456 (2012).
5. G. K. Mor, O. K. Varghese, M. Paulose, K. Shankar and C. A. Grimes, *Sol. Energy Mater.*, **90**, 2011 (2006).
6. C. A. Grimes, *J. Mater. Chem.,* **17**, 1451 (2007).
7. A. El Ruby Mohamed and S. Rohani, *Energy Environ. Sci.*, **4**, 1065 (2011).
8. G. Mor and C. Grimes, TiO_2 nanotube arrays-synthesis, properties and applications, Springer, New York (2009).
9. M. R. Hoffmann, S. T. Martin, W. Choi and D. W. Bahnemann, *Chem. Rev.*, **95**, 69 (1995).
10. W. Choi, A. Termin and M. R. Hoffmann, *Angew. Chem. Int. Ed.*, **33**, 1091 (1994).
11. X. Chen, L. Liu, Y. Y. Peter and S. S. Mao, *Science*, **331**, 746 (2011).
12. J. M. Macak, B. G. Gong, M. Hueppe and P. Schmuki, *Adv. Mater.*, **19**, 3027 (2007).
13. J. M. Macak, H. Tsuchiya, A. Ghicov, K. Yasuda, R. Hahn, S. Bauer and P. Schmuki, *Curr. Opin. Solid State Mater. Sci.*, **11**, 3 (2007).
14. Y. C. Nah, I. Paramasivam and P. Schmuki, *ChemPhysChem*, **11**, 2698 (2010).
15. X. Lu, G. Wang, T. Zhai, M. Yu, J. Gan, Y. Tong and Y. Li, *Nano Lett.*, **12**, 1690 (2012).
16. A. Zaleska, *Recent Pat. Eng.*, **2**, 157 (2008).
17. J. H. Park, S. Kim and A. J. Bard, *Nano Lett.*, **6**, 24 (2006).
18. F. Fabregat-Santiago, E. M. Barea, J. Bisquert, G. K. Mor, K. Shankar and C. A. Grimes, *J. Am. Chem. Soc.*, **130**, 11312 (2008).
19. Z. Zhang, M. N. Hedhili, H. Zhu and P. Wang, *Phys. Chem. Chem. Phys.*, **15**, 15637 (2013).
20. W. Liao, J. Yang, H. Zhou, M. Murugananthan and Y. Zhang, *Electrochim. Acta*, **136**, 310 (2014).
21. C. Xu, Y. Song, L. Lu, C. Cheng, D. Liu, X. Fang, X. Chen, X. Zhu and D. Li, *Nanoscale Res. Lett.*, **8**, 391 (2013).
22. W. Zhong, S. Sang, Y. Liu, Q. Wu, K. Liu and H. Liu, *J. Power Sources*, **294**, 216 (2015).
23. Q. Zheng, H.-J. Lee, J. Lee, W. Choi, N.-B. Park and C. Lee, *Chem. Eng. J.,* **249**, 285 (2014).
24. C. C. Raj and R. Prasanth, *J. Electrochem. Soc.*, **165**, E345 (2018).
25. C. Kim, S. Kim, J. Choi, J. Lee, J. S. Kang, Y.-E. Sung, J. Lee, W. Choi and J. Yoon, *Electrochim. Acta*, **141**, 113 (2014).
26. C. Kim, S. Kim, J. Lee, J. Kim and J. Yoon, *ACS Appl. Mater. Interfaces*, **7**, 7486 (2015).
27. Y. Yang, J. Liao, Y. Li, X. Cao, N. Li, C. Wang and S. Lin, *RSC Adv.*, **6**, 46871 (2016).
28. H. W. Jeong, K. J. Park, D. S. Han and H. Park, *Appl. Catal., B*, **226**, 194 (2018).
29. C. Kim, S. Lee, S. Kim and J. Yoon, *Electrochim. Acta*, **222**, 1578 (2016).
30. A. Zhang, F. Gong, Y. Xiao, X. Guo, F. Li, L. Wang, Y. Zhang and L. Zhang, *J. Electrochem. Soc.*, **164**, H91 (2017).
31. C. Kim, S. Kim, S. P. Hong, J. Lee and J. Yoon, *Phys. Chem. Chem. Phys.*, **18**, 14370 (2016).
32. Z. Li, Y. Ding, W. Kang, C. Li, D. Lin, X. Wang, Z. Chen, M. Wu and D. Pan, *Electrochim. Acta*, **161**, 40 (2015).
33. N. S. Peighambardoust, S. K. Asl, R. Mohammadpour and S. K. Asl, *Electrochim. Acta*, **270**, 245 (2018).
34. R. Vellacheri, H. Zhao, M. Mühlstädt, J. Ming, A. Al-Haddad, M. Wu, K. D. Jandt and Y. Lei, *Adv. Mater. Technol.*, **1**, 1600012 (2016).
35. D. D. Silva, I. Sánchez-Montes, P. Hammer and J. M. Aquino, *Electrochim. Acta*, **245**, 165 (2017).
36. T. Anwar, W. Li, R. U. R. Sagar, F. Nosheen, R. Singh, H. M. Jafri, K. Shehzad and L. Tongxiang, *J. Mater. Sci.*, **52**, 4323 (2017).
37. J. Radjenovic and D. L. Sedlak, *Environ. Sci. Technol.*, **49**, 11292 (2015).
38. J. Kim, C. Lee and J. Yoon, *Ind. Eng. Chem. Res.*, **57**, 11465 (2018).
39. S. Kim, C. Kim, J. Lee, S. Kim, J. Lee, J. Kim and J. Yoon, *ACS Sustainable Chem. Eng.*, **6**, 1620 (2018).
40. N. Liu, C. Schneider, D. Freitag, E. M. Zolnhofer, K. Meyer and P. Schmuki, *Chem. Eur. J.*, **22**, 13810 (2016).
41. H. Zhu, M. Zhao, J. Zhou, W. Li, H. Wang, Z. Xu, L. Lu, L. Pei, Z. Shi and S. Yan, *Appl. Catal., B*, **234**, 100 (2018).
42. L. Zhu, H. Ma, H. Han, Y. Fu, C. Ma, Z. Yu and X. Dong, *RSC Adv.*, **8**, 18992 (2018).
43. H. Zhou and Y. Zhang, *J. Phys. Chem. C,* **118**, 5626 (2014).
44. H. Zhou and Y. Zhang, *J. Power Sources*, **239**, 128 (2013).
45. V. Zwilling, E. Darque-Ceretti, A. Boutry-Forveille, D. David, M.-Y. Perrin and M. Aucouturier, *Surf. Interface Anal.*, **27**, 629 (1999).
46. V. Zwilling, M. Aucouturier and E. Darque-Ceretti, *Electrochim. Acta*, **45**, 921 (1999).
47. G. Mor, O. K. Varghese, M. Paulose, N. Mukherjee and C. A. Grimes, *J. Mater. Res.*, **18**, 2588 (2003).
48. Q. Cai, M. Paulose, O. K. Varghese and C. A. Grimes, *J. Mater. Res.*, **20**, 230 (2005).
49. G. K. Mor, K. Shankar, M. Paulose, O. K. Varghese and C. A. Grimes, *Nano Lett.*, **5**, 191 (2005).
50. J. M. Macak, K. Sirotna and P. Schmuki, *Electrochim. Acta*, **50**, 3679 (2005).
51. J. M. Macák, H. Tsuchiya and P. Schmuki, *Angew. Chem. Int. Ed.*, **44**, 2100 (2005).
52. L. Taveira, J. Macak, H. Tsuchiya, L. Dick and P. Schmuki, *J. Electrochem. Soc.*, **152**, B405 (2005).
53. S. P. Albu, A. Ghicov, J. M. Macak and P. Schmuki, *Phys. Status Solidi RRL*, **1**, R65 (2007).
54. K. Yasuda and P. Schmuki, *Electrochim. Acta*, **52**, 4053 (2007).
55. S. Bauer, S. Kleber and P. Schmuki, *Electrochem. Commun.*, **8**, 1321 (2006).
56. S. Berger, J. Kunze, P. Schmuki, D. LeClere, A. T. Valota, P. Skeldon and G. E. Thompson, *Electrochim. Acta*, **54**, 5942 (2009).
57. S. Li, G. Zhang, D. Guo, L. Yu and W. Zhang, *J. Phys. Chem. C*, **113**, 12759 (2009).
58. L. Hu, K. Huo, R. Chen, B. Gao, J. Fu and P. K. Chu, *Anal. Chem.*, **83**, 8138 (2011).
59. J. E. Houser and K. R. Hebert, *Nat. Mater.*, **8**, 415 (2009).

60. Q. A. S. Nguyen, Y. V. Bhargava, V. R. Radmilovic and T. M. Devine, *Electrochim. Acta*, **54**, 4340 (2009).
61. A. Valota, D. LeClere, P. Skeldon, M. Curioni, T. Hashimoto, S. Berger, J. Kunze, P. Schmuki and G. Thompson, *Electrochim. Acta*, **54**, 4321 (2009).
62. J.-L. Delplancke, A. Garnier, Y. Massiani and R. Winand, *Electrochim. Acta*, **39**, 1281 (1994).
63. D. R. Zhang, X. Z. Jin and J. H. Li, *Master. Chem. Phys.*, **176**, 68 (2016).
64. J. Arbiol, J. Cerda, G. Dezanneau, A. Cirera, F. Peiro, A. Cornet and J. Morante, *J. Appl. Phys.*, **92**, 853 (2002).
65. D. Reyes-Coronado, G. Rodríguez-Gattorno, M. Espinosa-Pesqueira, C. Cab, R. d. de Coss and G. Oskam, *Nanotechnology*, **19**, 145605 (2008).
66. G. K. Mor, O. K. Varghese, M. Paulose and C. A. Grimes, *Adv. Funct. Mater.*, **15**, 1291 (2005).
67. V. Mahajan, M. Misra, K. Raja and S. Mohapatra, *J. Phys. D: Appl. Phys.*, **41**, 125307 (2008).
68. M. Kunat and U. Burghaus, *Surf. Sci.*, **544**, 170 (2003).
69. S. Funk and U. Burghaus, *Catal. Lett.*, **118**, 118 (2007).
70. S. K. Deb and S. Cells, *Sol. Energy Mater.*, **92**, 245 (2008).
71. F. Hu, F. Ding, S. Song and P. K. Shen, *J. Power Sources*, **163**, 415 (2006).
72. K. Nakata and A. Fujishima, *J. Photochem. Photobiol., C*, **13**, 169 (2012).
73. S.-Y. Lee and S.-J. Park, *J. Ind. Eng. Chem.*, **19**, 1761 (2013).
74. Z. Zhang, L. Zhang, M. N. Hedhili, H. Zhang and P. Wang, *Nano Lett.*, **13**, 14 (2012).
75. G. Wang, H. Wang, Y. Ling, Y. Tang, X. Yang, R. C. Fitzmorris, C. Wang, J. Z. Zhang and Y. Li, *Nano Lett.*, **11**, 3026 (2011).
76. V. Etacheri, C. Di Valentin, J. Schneider, D. Bahnemann and S. C. Pillai, *J. Photochem. Photobiol., C*, **25**, 1 (2015).
77. M. Grätzel, *Inorg. Chem.*, **44**, 6841 (2005).
78. K. Zhu, N. R. Neale, A. Miedaner and A. J. Frank, *Nano Lett.*, **7**, 69 (2007).
79. P. Roy, D. Kim, K. Lee, E. Spiecker and P. Schmuki, *Nanoscale Res. Lett.*, **2**, 45 (2010).
80. A. Kar, K. Raja and M. Misra, *Surf. Coat. Technol.*, **201**, 3723 (2006).
81. N. K. Shrestha, J. M. Macak, F. Schmidt-Stein, R. Hahn, C. T. Mierke, B. Fabry and P. Schmuki, *Angew. Chem. Int. Ed.*, **48**, 969 (2009).
82. Y. Y. Song, P. Roy, I. Paramasivam and P. Schmuki, *Angew. Chem. Int. Ed.*, **49**, 351 (2010).
83. J. Lee, D. H. Kim, S.-H. Hong and J. Y. J. S. Jho, *Sens. Actuators, B: Chem.*, **160**, 1494 (2011).
84. I.-D. Kim, A. Rothschild, B. H. Lee, D. Y. Kim, S. M. Jo and H. L. Tuller, *Nano Lett.*, **6**, 2009 (2006).
85. S. Berger, A. Ghicov, Y.-C. Nah and P. Schmuki, *Langmuir*, **25**, 4841 (2009).
86. T. Yamase, *Chem. Rev.*, **98**, 307 (1998).
87. H. Zhou and Y. Zhang, *J. Phys. Chem. C*, **118**, 5626 (2014).
88. W.-D. Zhu, C.-W. Wang, J.-B. Chen, Y. Li and J. Wang, *Appl. Surf. Sci.*, **301**, 525 (2014).
89. C. Xue, S. Hu, Q. Chang, N. Li, Y. Wang, W. Liu and J. Yang, *J. Mater. Sci.*, **53**, 9742 (2018).
90. H. Sierra-Uribe, J. E. Carrera-Crespo, A. Cano, E. M. Córdoba-Tuta, I. González and P. Acevedo-Peña, *J. Solid State Electrochem.*, **22**, 1881 (2018).
91. K. Du, G. Liu, M. Li, C. Wu, X. Chen and K. Wang, *Electrochim. Acta*, **210**, 367 (2016).
92. M. Xing, W. Fang, M. Nasir, Y. Ma, J. Zhang and M. Anpo, *J. Catal.*, **297**, 236 (2013).
93. J. Song, M. Zheng, X. Yuan, Q. Li, F. Wang, L. Ma, Y. You, S. Liu, P. Liu and D. Jiang, *J. Mater. Sci.*, **52**, 6976 (2017).
94. L. Zhang, H. Cao, Q. Pen, L. Wu, G. Hou, Y. Tang and G. Zheng, *Electrochim. Acta*, **283**, 1507 (2018).
95. M. Salari, K. Konstantinov and H. K. Liu, *J. Mater. Chem.*, **21**, 5128 (2011).
96. H. Wu, D. Li, X. Zhu, C. Yang, D. Liu, X. Chen, Y. Song and L. Lu, *Electrochim. Acta*, **116**, 129 (2014).
97. G. Zhu, T. Lin, X. Lü, W. Zhao, C. Yang, Z. Wang, H. Yin, Z. Liu, F. Huang and J. Lin, *J. Mater. Chem. A*, **1**, 9650 (2013).
98. J. Liu, M. Dai, J. Wu, Y. Hu, Q. Zhang, J. Cui, Y. Wang, H. H. Tan and Y. Wu, *Sci. Bulletin*, **63**, 194 (2018).
99. M. Salari, S. H. Aboutalebi, K. Konstantinov and H. K. Liu, *Phys. Chem. Chem. Phys.*, **13**, 5038 (2011).
100. M. S. Kim, T.-W. Lee and J. H. Park, *J. Electrochem. Soc.*, **156**, A584 (2009).
101. Q. Li, Z. Xia, S. Wang, Y. Zhang and Y. Zhang, *J. Solid State Electrochem.*, **21**, 2177 (2017).
102. N. A. Samsudin, Z. Zainal, H. N. Lim, Y. Sulaiman, S.-K. Chang, Y.-C. Lim, M. Amin and W. Nadrah, *J. Nanomater.*, **2018**, 1 (2018).
103. J. Duan, H. Hou, X. Liu, C. Yan, S. Liu, R. Meng, Z. Hao, Y. Yao and Q. Liao, *J. Porous Mater.*, **23**, 837 (2016).
104. C. Zhang, J. Xing, H. Fan, W. Zhang, M. Liao and Y. Song, *J. Mater. Sci.*, **52**, 3146 (2017).
105. H. Zhou and Y. Zhang, *J. Power Sources*, **272**, 866 (2014).
106. Y. Qin, J. Zhang, Y. Wang, X. Shu, C. Yu, J. Cui, H. Zheng, Y. Zhang and Y. Wu, *RSC Adv.*, **6**, 47669 (2016).
107. J. Duan, H. Hou, X. Liu, S. Liu, Q. Liao and Y. Yao, *Ceram. Int.*, **42**, 16611 (2016).
108. J. Duan, H. Hou, X. Liu, Q. Liao, S. Liu and Y. Yao, *Ionics*, **23**, 3037 (2017).
109. D. Pletcher and F. C. Walsh, Industrial electrochemistry, Springer Science & Business Media (2012).
110. J. Lipkowski and P. N. Ross, The electrochemistry of novel materials, VCH Publishers (1994).
111. A. Fujishima, Y. Einaga, T. N. Rao and D. A. Tryk, Diamond electrochemistry, Elsevier (2005).
112. J. Kim, C. Kim, S. Kim and J. Yoon, *J. Ind. Eng. Chem.*, **66**, 478 (2018).
113. Y. Yang and M. R. Hoffmann, *Environ. Sci. Technol.*, **50**, 11888 (2016).
114. Y. Yang, L. C. Kao, Y. Liu, K. Sun, H. Yu, J. Guo, S. Y. H. Liou and M. R. Hoffmann, *ACS Catal.*, **8**, 4278 (2018).
115. A. Ahmadi and T. Wu, *Environ. Sci.: Water Res. Technol.*, **3**, 534 (2017).
116. Y. Shi, Z. Lu, L. Guo, Z. Wang, C. Guo, H. Tan and C. Yan, *Int. J. Hydrogen Energy*, **43**, 9133 (2018).
117. J. Han, H. Choi, G. Lee, Y. Tak and J. Yoon, *J. Electrochem. Sci. Technol.*, **7**, 76 (2016).
118. H. Maltanava, S. Poznyak, M. Starykevich and M. Ivanovskaya, *Electrochim. Acta*, **222**, 1013 (2016).

119. W. Liao, M. Murugananthan and Y. Zhang, *Phys. Chem. Chem. Phys.*, **17**, 8877 (2015).
120. X. Zhang, B. Zhang, D. Huang, H. Yuan, M. Wang and Y. Shen, *Carbon*, **80**, 591 (2014).
121. L. Yu, M. Li, C. Huang, Y. Zhang, J. He, X. Zhou and H. Zhu, *Mater. Lett.*, **216**, 239 (2018).
122. M. S. Koo, K. Cho, J. Yoon and W. Choi, *Environ. Sci. Technol.*, **51**, 6590 (2017).